LAWRENCE
LIVERMORE
NATIONAL
LABORATORY

LLNL-JRNL-742926

Influence of Argon Impurities on the Elastic Scattering of X-Rays from Imploding Beryllium Capsules

A. M. Saunders, D. A. Chapman, D. O. Gericke, S. H. Glenzer, A. L. Kritcher, O. L. Landen, M. Schoff, R. W. Falcone, T. Doeppner, C. Schuldberg

December 7, 2017

High Energy Density Physics

Disclaimer

Influence of Argon Impurities on the Elastic Scattering of X-Rays from Imploding Beryllium Capsules

A. M. Saunders[a], D. A. Chapman[b,c], A. L. Kritcher[d], M. Schoff[e], C. Shuldberg[e], O. L. Landen[d], S. H. Glenzer[f], R. W. Falcone[a], D. O. Gericke[c], T. Döppner[d]

[a] *Physics Department, University of California Berkeley, Berkeley, California 94709, USA*
[b] *AWE plc, Aldermaston, Reading, RG7 4PR, United Kingdom*
[c] *Centre for Fusion, Space and Astrophysics, Department of Physics, University of Warwick, Coventry CV4 7AL, United Kingdom*
[d] *Lawrence Livermore National Laboratory, 7000 East Avenue, Livermore, CA 94551, USA*
[e] *General Atomics, 3550 General Atomics Ct., San Diego, CA 92121, USA*
[f] *SLAC National Accelerator Laboratory, 2575 Sand Hill Road, Menlo Park, CA 94025, USA*

Abstract

We investigate the effect of argon impurities on the elastic component of x-ray scattering spectra taken from directly driven beryllium capsule implosions at the Omega laser. The plasma conditions were obtained in a previous analysis (A. L. Kritcher *et al.*, Phys. Rev. Lett., **107**, 015002 (2011)) by fitting the inelastic scattering component. We show that the known argon impurity in the beryllium modifies the elastic scattering due to the larger number of bound electrons. We indeed find significant deviations in the elastic scattering from roughly 1 atomic % argon contained in the beryllium. With knowledge of the argon impurity fraction, we use the elastic scattering component to determine the charge state of the compressed beryllium, as the fits are rather insensitive to the argon charge state. Finally, we discuss how doping small fractions of mid- or high-Z elements into low-Z materials could allow ionization balance studies in dense plasmas.

Keywords: warm-dense-matter, dense plasmas, x-ray Thomson scattering, ionization balance

Email address: saunders@berkeley.edu (A. M. Saunders)

1. Introduction

Studying matter with extreme energy densities in laboratory experiments improves our understanding of astrophysical objects [1, 2, 3, 4] and aides in the quest to demonstrate inertial confinement fusion in the laboratory [5, 6, 7]. X-ray Thomson scattering (XRTS) provides a powerful method to characterize plasmas at such extreme conditions by measuring key plasma parameters such as temperature, density, and ionization [8]. In recent years, ionization potential depression (IPD) has become a topic of active scientific debate as early experiments reported deviations from widely used ionization models [9, 10, 11, 12, 13]. However, these results have come under question due to potentially inconsistent treatments of atomic potentials and simplified atomic models used to infer the ionization state of the materials [14, 15]. It is therefore of interest to develop experimental techniques that directly measure the ionization state of dense plasmas. XRTS measures the ionization state from the ratio of elastic-to-inelastic scattering, but also requires a good understanding of the modeling underlying the elastic scattering signal strength.

In this paper, we assess the impact of a small (around one percent by number density) argon impurity fraction on the elastic scattering signal strength from beryllium plasmas. Our results demonstrate that careful impurity characterization is important for accurate ionization measurements using the elastic component of XRTS. Moreover, we show that intentional doping of mid- or high-Z elements into low-Z samples might provide a path towards studying ionization potential lowering of higher-Z elements, which might be not possible otherwise due to the high opacity of the pure mid-Z sample.

In an XRTS experiment, a collimated x-ray source impinges on a sample, and a spectrometer spectrally resolves the scattered photons at a desired scattering angle. XRTS spectra typically consist of two major components: elastically scattered photons with the frequency of the original x-ray source and inelastically scattered photons that are down-shifted in frequency. The Compton-shifted profile of inelastically scattered x-rays can be analyzed to return the sample's electron density and electron temperature. The ratio of elastically to inelastically scattered x-rays relates to the number of tightly bound versus free electrons, and thus reflects the ionization state.

The use of inelastically scattered x-rays to infer electron temperature and

density is well documented. Several experiments on beryllium samples used large scattering angles to probe the properties of individual electrons and to measure electron temperatures and densities through analysis of the shape of the Compton peak [16, 17, 18]. Forward-scattering geometries probe the collective behavior of the electrons, i.e. plasmons [19, 20, 21]. The elastic scattering component is often used to infer ion properties such as the static structure factor [22, 23, 24, 25] or the associated screening properties [26]. The Rayleigh weight, which reflects the integral of the elastic scattering peak, relates to the number of tightly bound electrons, which allows investigation of the ionization balance. Recent XRTS experiments found higher ionization states than predicted for a large range of conditions [12, 27].

The static structure factors, atomic form factors, screening properties, and ionization balance measured by XRTS are well suited for a comparison with theoretical modeling. While much progress has been achieved in recent years, there remains a significant need for additional experimental validation of theoretical predictions. In particular, experimental measurements of the properties of warm dense matter are needed for integrated modeling of inertial confinement fusion experiments [5, 6, 7] and astrophysical objects [1, 2, 3, 4]. A particularly interesting question is the behavior of elemental mixtures and how the different components interact with each other and affect x-ray scattering. The mutual interactions and arrangements of different species are predicted to yield signatures in the XRTS spectra. Moreover, one needs to ensure that impurities do not invalidate the results obtained.

In the following sections, we perform a reanalysis of in-flight XRTS data from beryllium capsule implosions that were driven by the OMEGA laser [18]. After reviewing the experiment, its data, and the description of XRTS spectra from multi-component systems, we apply our analysis with special focus on the elastic scattering feature. We find a significant contribution from the argon component to the elastic scattering amplitude, which allows us to determine the argon content of the samples. We also find a strong decrease of the ratio of elastic to inelastic scattering as the capsule implodes, indicating an increasing ionization during compression. Due to the large scattering angle, the data are much more sensitive to the beryllium ionization than to the ionization of the argon impurities. Finally, we give an outlook on possible ways to investigate the ionization of mid-Z ions in high energy density conditions, where highly compressed beryllium provides an environment of high free electron densities and moderate temperatures.

2. Overview of Experimental Setup and Data Collection

The experimental data discussed here were obtained from an XRTS experiment undertaken at the OMEGA laser [18]. In this campaign, several time-resolved XRTS spectra were collected from imploding beryllium shells. The previous analysis focused on the inelastic scattering feature, that is the Compton-shifted response of the free electrons and scattering by bound-free transitions. Fitting this feature allowed for the determination of the electron temperatures and free-electron densities at different times, as well as an ionization state of the beryllium from the long tail on the Compton-peak, which derives from scattering from loosely bound electrons [18]. Here, we consider the information contained in the elastic scattering feature to gain insights into the ion properties, mainly the ion charge state, and the contribution of the argon contamination in the beryllium.

Figure 1 summarizes the setup of the experiment. The part on the top-left shows a schematic of the cone-in-shell design used for the XRTS measurements: 36 laser beams impinged directly on a spherical beryllium shell for 2 ns. The strong laser-ablation accelerated the spherical sample symmetrically towards the center. Nine additional laser beams heated the zinc to create a pulse of He-α line radiation at 9.0 keV that was used as the probe. The x-rays scattered from the sample and were collected at a scattering angle of 135° by a Bragg-crystal spectrometer that consists of a highly oriented pyrolitic graphite crystal connected to a gated multichannel plate detector. The zinc foil was glued on the inside of a gold half-cone that served to block the direct line of sight to the spectrometer. A photo of the beryllium target, the backlighter foil, and the gold shield is shown in the bottom-left of Fig. 1. The lower right of Fig. 1 contains results from radiation-hydrodynamics simulations for the implosion. Here, the density increase to the laser drive is shown together with the laser power and the probing times. All times refer to $t = 0$ being set by the beginning of the laser drive, and peak compression is predicted to occur around 5 ns.

The beryllium targets were 40 µm thick spherical shells with an outer diameter of 860 µm and a density of 1.85 g cm^{-3}. They were also glued directly onto the gold cone, as seen in Figure 1. The beryllium contained an argon impurity fraction, μ_{Ar}, as a result of the beryllium sputtering manufacturing process. Argon acts as the sputter gas and participates in the ion-assisted

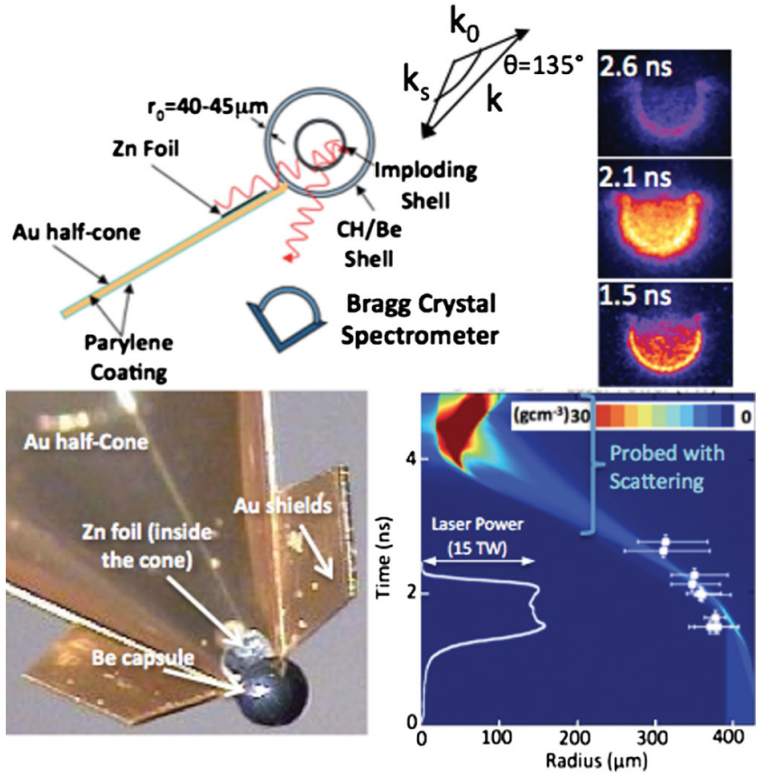

Figure 1: Experimental setup of the experiment as presented in Ref. [18]. The top shows the schematic of the experiment and images of the x-ray emission from the sample as it imploded. The bottom displays a photo of the cone-in-shell target as well as outputs from radiation-hydrodynamic modeling of the imploding beryllium capsule. Reprinted figure with permission from A. L. Kritcher, T. Döppner, C. Fortmann, T. Ma, O. L. Landen, R. Wallace, and S. H. Glenzer, Phys. Rev. Lett., **107**, 015002 (2011). Copyright 2011 by the American Physical Society. https://doi.org/10.1103/PhysRevLett.107.015002

coating of the capsules, which breaks up the columnar structure of beryllium and results in leak-tight capsules. The sputtered capsules usually contain an atomic argon impurity fraction of $\mu_{Ar} = 0.5 - 2.0\%$. In this paper, impurity concentrations are described by atomic percent (at.%), which describes the fractional ion density of a species. The exact percentage of argon was not characterized in the original experiment. Other impurities in the Be include oxygen, at less than 1 at.% from oxidation of the outer layers of the shells, and trace amounts of iron at roughly 60 parts per million. However, oxygen and iron at these concentrations do not contribute enough bound electrons

to affect the elastic scattering signal strength; the remainder of this paper focuses on the dominating effects of the argon impurity.

XRTS spectra were taken at several times along the implosion trajectory of the beryllium shell [18]. Without accounting for the argon, the strength of the elastic feature could not be reproduced. Thus, only the inelastic component of each scattering profile was analyzed. Nevertheless, the electron temperatures and densities could be determined from the Compton feature at several times during the compression. Here, we will focus on two cases: the spectrum taken at $t = 3.1\,\mathrm{ns}$ yielding an electron temperature of $T_e = (14 \pm 3)\,\mathrm{eV}$ and a free electron density of $n_e = (1.1 \pm 0.3) \times 10^{24}\,\mathrm{cm}^{-3}$, and the spectrum recorded $t = 5.7\,\mathrm{ns}$ after the beginning of the laser drive where $T_e = (41 \pm 5)\,\mathrm{eV}$ and $n_e = (1.9 \pm 0.5) \times 10^{24}\,\mathrm{cm}^{-3}$ was determined [18]. While the first spectrum is one of the earliest, the second is close to peak compression. Based on the reported plasma parameters, we now extend the analysis to the elastic feature of the spectra by accounting for the argon impurity in the sample.

3. XRTS Theory for Multi-Component Systems

We give a brief summary of the relevant theory for XRTS with special emphasis on systems containing multiple ion species [28]. A full account of all mutual correlations is necessary here, as we expect strongly coupled ions and a significant difference between the charge states of beryllium and argon.

In an XRTS experiment, x-rays scatter into the full solid angle carrying distinct information from the plasma target. The scattered power per frequency and per solid angle can be written as [8]

$$\frac{d^2P}{d\Omega d\omega} = r_0^2 \frac{1}{2}\left(1 + \cos^2\theta\right)\left(\frac{\omega_s}{\omega_i}\right)^2 N I_0 S(k,\omega)\,, \tag{1}$$

where P is the scattered power, r_0 is the classical electron radius, θ is the scattering angle, N is the number of scatterers, and I_0 is the intensity incident on the target. The term including $\cos^2\theta$ describes polarization dependence of unpolarized light. $\hbar\omega = \hbar(\omega_i - \omega_s)$ is the change in the photon's energy where ω_i and ω_s are the frequencies of the incident and the scattered photons, respectively. k denotes the magnitude of the wave vector change during the scattering and is determined by the scattering angle and incident frequency, by $k = \frac{2}{c}\omega_i \sin\theta/2$.

The total dynamic electron structure factor, $S(k,\omega)$, includes the properties of the correlated system. As the electrons interact with the ions, the structure factor contains information on the electron response and on the behavior of the ions as shown by the widely applied decomposition derived by Chihara [29, 30]

$$S(k,\omega) = W_R(k)\,\delta(\omega) + W_C^{ff}(k,\omega) + W_C^{bf}(k,\omega)\,. \tag{2}$$

Here, the first term denotes the near-elastic (Rayleigh) scattering that can be linked to the ion properties. The second and third terms are the inelastic (Compton-shifted) contributions due to the dynamic response of the free electrons and due to bound-free transitions, respectively. The latter two can be calculated on the basis of standard approximations [8]. On this basis, Kritcher *et al.* [18] obtained the basic plasma properties mentioned above that we will use here.

The elastic scattering contribution, i.e. the first term in Eq. (2), contains information about the ionic structure. In a system with multiple ion species, all mutual arrangements must be taken into account. Thus, it is necessary to use a multi-component description of the weight of the Rayleigh feature [28]

$$W_R(k) = \sum_{a,b} \sqrt{x_a x_b}\,[f_a(k) + q_a(k)]\,[f_b(k) + q_b(k)]\,S_{ab}(k)\,. \tag{3}$$

Here, the elastic scattering is determined by the individual form factors for each species, $f_a(k)$, the individual screening contributions, $q_a(k)$, the fractions of the different ions species, $x_a = n_a/\sum_a n_a$, the number densities, n_a, and all combinations of partial ionic structure factors, $S_{ab}(k)$. In this formula, the argon impurity μ_{Ar} is represented by the fractional number density of one of the species, i.e. x_a. Estimates of the partial structure factors may be obtained from, e.g., the multi-component hypernetted-chain (HNC) approach [31, 32].

4. Analysis of the Rayleigh Weights

To investigate the weight of the elastic scattering feature, we fit several raw line-outs of the spectral data with the sums of two Gaussians. One Gaussian fits the elastic feature and the other fits the inelastic feature; the heights and widths of the Gaussians are scaled relatively to each other until the sum of the two Gaussians minimizes the fitting residuals from the data.

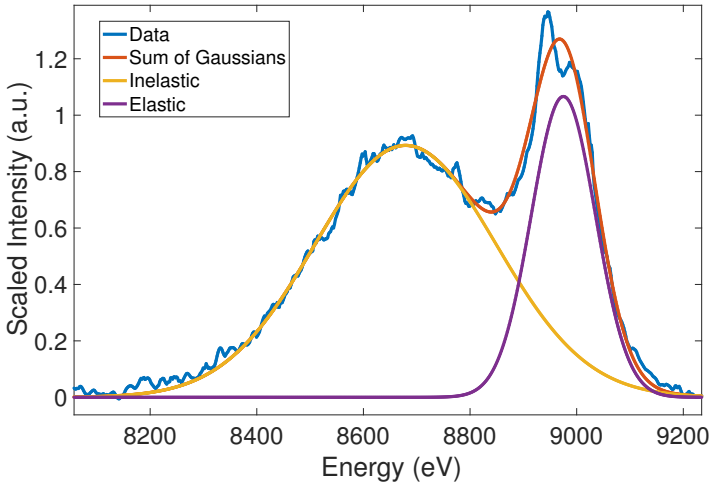

Figure 2: (Color online) XRTS spectrum taken at $t = 5.7$ ns after the start of the laser drive [18]. Both the elastic scattering feature on the right as well as the inelastic feature on the left were fitted by Gaussian functions. While the special shape of the zinc He-α line (see shape of the elastic feature in the experimental data) is not accounted for, this procedure generates the correct weights under the two features.

We chose to model the probe spectrum as a Gaussian due to the limited spectral resolution of the instrument, and to simplify the initial analysis. An example of the results is presented in Figure 2. The deviation at the top of the elastic feature is due to the double peak structure of the zinc He-α incident source, with lines at 8950 and 8999 eV. Besides this feature, fits with two Gaussians represents the data quite well.

The integrals of the Gaussians define the weight of the total inelastic scattering feature and the weight of the Rayleigh peak $W_R(k)$, respectively. The ratio of the two areas is a good measure of their relative strengths and, moreover, independent of absolute signal levels. We thus analyze the time-dependence of the implosion via the ratio of elastic to inelastic scatter.

Figure 3 shows the ratios of weights for the elastic and inelastic scattering features for a number of spectra taken at different times during the implosion [18]. The spread in ratios at a given time could be in part due to variations in crystal and framing camera flat fielding, but the trend stands out above the noise in the data; the elastic to inelastic ratio decreases with time by almost 40% as the capsule compresses. This cannot be explained by the heating and compression alone; either beryllium or argon ionization must also contribute

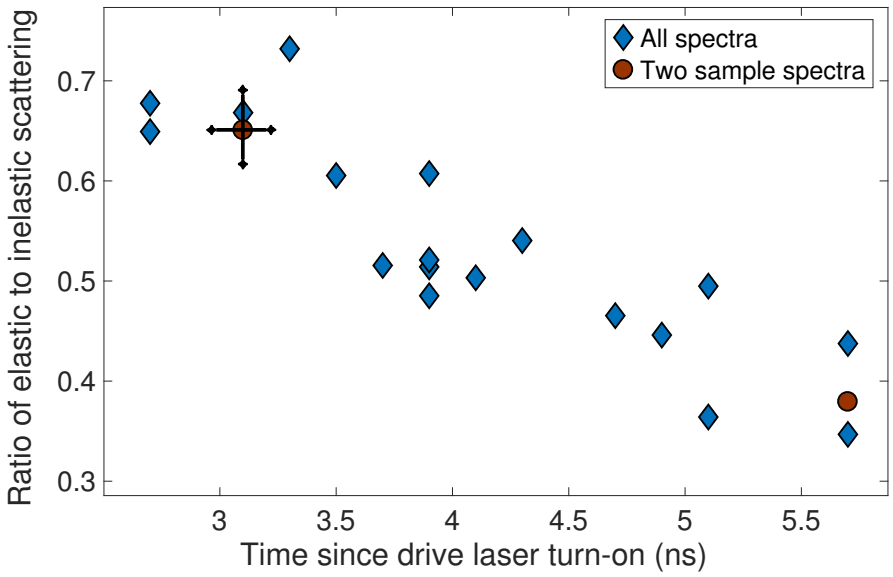

Figure 3: (Color online) Ratio of elastic to inelastic scattering strength versus time for spectra taken by Kritcher *et al.* [18]. Each diamond represents the ratio from one spectrum. The laser drive turns on at $t = 0$ and turns off after $t = 2$ ns, with peak compression reached at 5.7 ns. Here, we focus on the two spectra marked by red circles (early during the implosion and near peak compression). The red data point at 3.1 ns shows representative error bars.

to this drop in elastic scattering.

To quantify the effects of compression and ionization, we generated theoretical predictions for the scattering spectra of a sample consisting of beryllium and 0.75% argon. All the theoretical calculations of the scattered power spectra shown in this work are based on the MCSS code [33, 34]. The dynamic contributions, i.e. the free-free and bound-free terms, are well documented in the literature. The elastic scattering contribution to the theoretical power spectra have also been calculated using various commonly-used simple models but, due to its central role in our present work, warrants additional explanation. For the structure of the bound electrons (ionic form factor), we use the usual screened hydrogenic approximation. Here, the effective nuclear charge for each occupied sub-shell is given by the well-known values tabulated by Pauling and Sherman [35]. The structure of the screening cloud has been treated in the finite-wavelength screening formalism [26], which accounts for

the short-range Friedel-like density oscillations and also includes a strong coupling correction to the static screening function [36]. The electron-ion potential is considered to be Coulomb-like, with an effective ionic charge consistent with the mean ionization state for each species (Be or Ar). Finally, the spatial correlations of the ions modulating the amplitude of the Rayleigh signal is described using the multi-component HNC approach [31]. For this part of the calculation only the ions are considered (no explicit electron-ion correlations are used) and the inter-ion potential is treated with a statically screened Yukawa interaction; the effective charges of the ions are again assumed to be consistent with the mean ionization states of the components of the plasma. Improvements on these simple models are widely known, e.g. using a pseudo-potential for the electron-ion and ion-ion interactions, although these invariably require additional fitting constants and/or material-specific information which would introduce undesirable extra model uncertainty. The suite of models used here offers a reasonable compromise between physical accuracy and numerical economy and enables the large parameter scans required to undertake the rigorous statistical analysis which underlines our present results.

To represent the x-ray source function, we used a measured Zn He-α spectrum, broadened by the scattering source size. Our theoretical predictions show that at a scattering angle of 135°, the change in plasma conditions from $T = 14\,\mathrm{eV}$ and $n_e = 1.1 \times 10^{24}\,\mathrm{cm}^{-3}$ to $T = 41\,\mathrm{eV}$ and $n_e = 1.9 \times 10^{24}\,\mathrm{cm}^{-3}$ accounts for a 20% decrease of the ratio of elastic to inelastic scattering if the ionization of both ion species is kept constant. Thus, it is reasonable to attribute the remainder of the observed decrease in elastic-inelastic signal strength to ionization. Specifically, the mean ionization of either the Be or the Ar may account for our observations. We now undertake a careful analysis of our experimental data to quantitatively understand the relative sensitivity of the spectra to ionization of either component.

Our theoretical predictions also demonstrate that the elastic scattering signal strength cannot be reproduced without accounting for the argon impurity fraction. Figure 4 shows an example for the experimental conditions at $t = 3.1$ ns. To set the ionization, we ran simulations in the atomic kinetics and radiation transport code Cretin; for all available continuum lowering models [37], the code predicted an ionization state of $Z_{Be} = 2.0$ and $Z_{Ar} = 8.0$ over all combinations of plasma conditions relevant to the spectrum at 3.1 ns [18]. Using the aforementioned values, the MCSS calculations show that adding only 0.75 at.% Ar to the sample increases the elastic scattering by

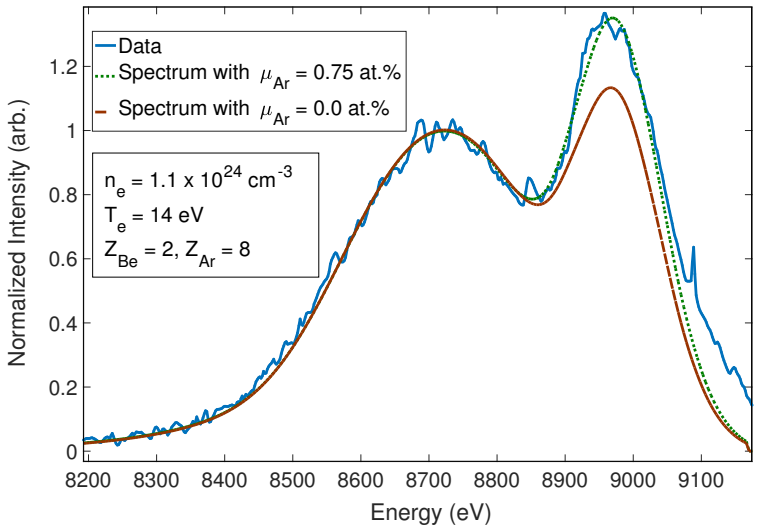

Figure 4: (Color online) An XRTS spectrum taken at 3.1 ns [18] compared to two theoretically generated spectra. Both predictions use a source-broadened Zn He-α source, a temperature of $T = 14\,\mathrm{eV}$, an electron density of $1.1 \times 10^{24}\,\mathrm{cm}^{-3}$, and a scattering angle of 135°. They differ only in the assumed argon content: the simulation represented by the solid line neglects the argon in the sample, while the dashed line is a simulation that assumes an argon impurity of 0.75 at.%.

20% and enables us to match the experimental observation. Thus, it is of great importance to quantify carefully the argon content in the sample and the sensitivity of the elastic signal strength to argon and beryllium ionization. In the following, we will focus on the spectra taken at 3.1 ns and at 5.7 ns, which show a large difference in the ratio of elastic to inelastic scattering.

Figure 5 shows the deviation of model spectra to the measured elastic scattering feature of the spectrum taken at 3.1 ns (χ^2 analysis). Here, n_e, T_e, and Z_{Be} are kept fixed to the values reported in Ref. [18] and only the argon fraction and argon ionization state are varied. The χ^2 analysis reveals that the elastic scattering strength is not sensitive to argon ionization until the argon ionizes into to the L-shell, i.e. for $Z_{Ar} \geq 8$. The Compton energy (244 eV) is large enough such that all M-shell electrons scatter inelastically into the bound-free contribution. Only for smaller scattering angles of $\theta \leq 55°$ ($k \leq 4$ Å^{-1}), would we expect M-shell electrons to participate in the elastic scattering. Figure 5 also demonstrates that 0.75 ± 0.2 at.% of argon reproduces the measured elastic scattering signal strength if we assume argon does

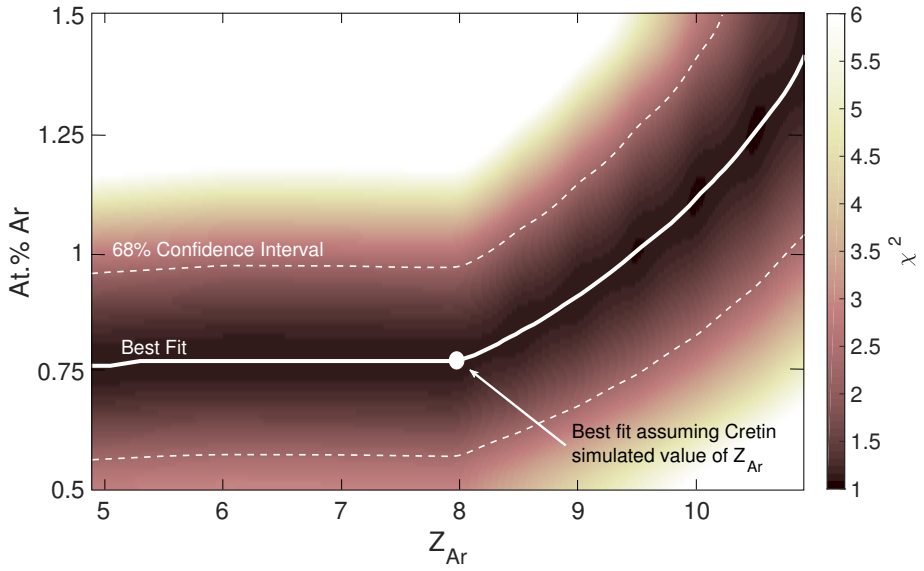

Figure 5: (Color online) (a) χ^2 analysis of the elastic scattering feature of the spectrum at 3.1 ns, varying argon impurity fraction and argon ionization. All fits use assume $Z_{Be} = 2$, $T_e = 14\,\text{eV}$, and $n_e = 1.1 \times 10^{24}\,\text{cm}^{-3}$, as reported in Ref. [18]. Since the Ar ionization is reported to be $Z_{Ar} = 8$ by Cretin simulations at these plasma conditions, the best fit is obtained for an Ar impurity fraction of $0.75 \pm 0.20\%$.

not ionize into the L-shell. This finding is consistent throughout the conditions probed (and also for different times - not shown) and agrees with our knowledge about the capsules; the producer of the capsules, General Atomics, now regularly measures an argon impurity fraction of 0.5 to 2.0 at.% in the capsules they produce. At the time this experiment was performed, however, the regular reporting of argon impurities had not yet been implemented. We thus use our experimental finding and fix μ_{Ar} to 0.75 at.% for the following analysis and discussion of the XRTS spectrum at 5.7 ns.

The spectrum at 5.7 ns was taken very close to peak compression, when the sample was heated to $T = 41\,\text{eV}$ with a free electron density of $n_e = 1.9 \times 10^{24}\,\text{cm}^{-3}$. Fig. 6 shows the χ^2 analysis of model spectra to the elastic feature of the spectrum at 5.7 ns that vary argon and beryllium ionization; the inelastic feature is again reproduced by using the previously inferred plasma parameters [18]. Similarly to Figure 5, the results show that the elastic scattering strength is sensitive to both beryllium and argon ionization if the

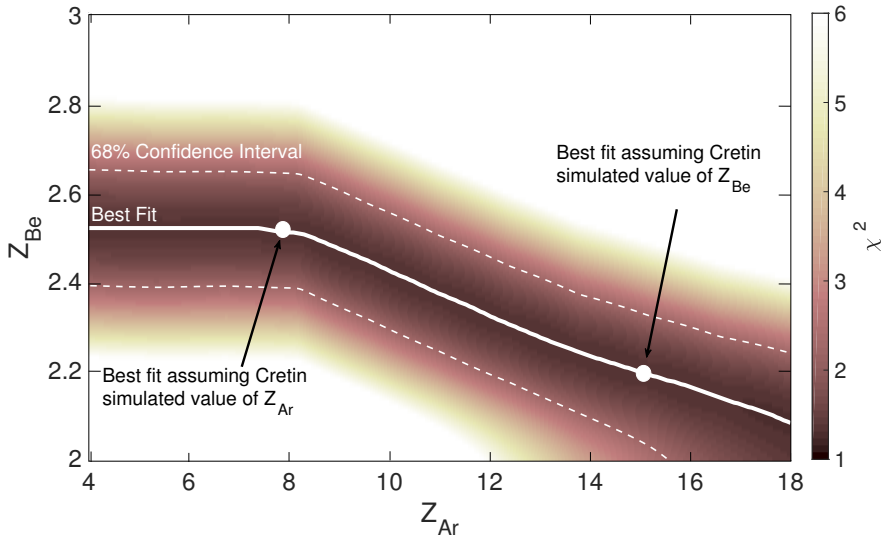

Figure 6: (Color online) χ^2 analysis of the elastic scattering strength in the spectrum at 5.7 ns, varying beryllium ionization and argon ionization. Best fits at each Ar ionization state are shown as the bold white line, with 1σ contours indicated by the dashed white lines. All fits assume 0.75 at.% of argon, $T_e = 41$ eV, and $n_e = 1.9 \times 10^{24}$ cm^{-3}. The best fit is found for $Z_{Be} = 2.5 \pm 0.2$ when the Ar ionization is constrained to $Z_{Ar} \leq 8$. The white dots represent the positions of Cretin simulations for Z_{Be} and the required Z_{Ar} to match, and vice versa. $Z_{Ar} \geq 9.5$ is unphysical, for details see text.

argon ionizes into its L-shell, i.e. for $Z_{Ar} > 8$. The predictions for ionization balance vary more at these hotter and denser conditions than they do at the conditions at 3.1 ns.

Figure 7 shows Cretin simulations of both beryllium (a) and argon (b) ionization versus temperature with different models for ionization potential depression (IPD), assuming a constant electron density of 1.9×10^{24} cm^{-3} and $\mu_{Ar} = 0.75$ at.%. At the previously reported temperature of 41 eV, Cretin predicts that argon just begins to ionize into its L-shell, to an average charge state between $Z_{Ar} = 8.01$ and 8.15, depending on the model used for continuum lowering. If we constrain Z_{Ar} to these conditions, a beryllium ionization of $Z_{Be} = 2.5$ reproduces the elastic scattering strength, as indicated by the first white marker in Figure 6. This significant ionization into the K-shell of beryllium is higher than the Cretin predicted value of $Z_{Be} = 2.2$ (cf. Figure 6(a)). The original analysis of the inelastic feature also found $Z_{Be} = 2.5$ from fitting the red-shifted tail on the Compton peak caused by

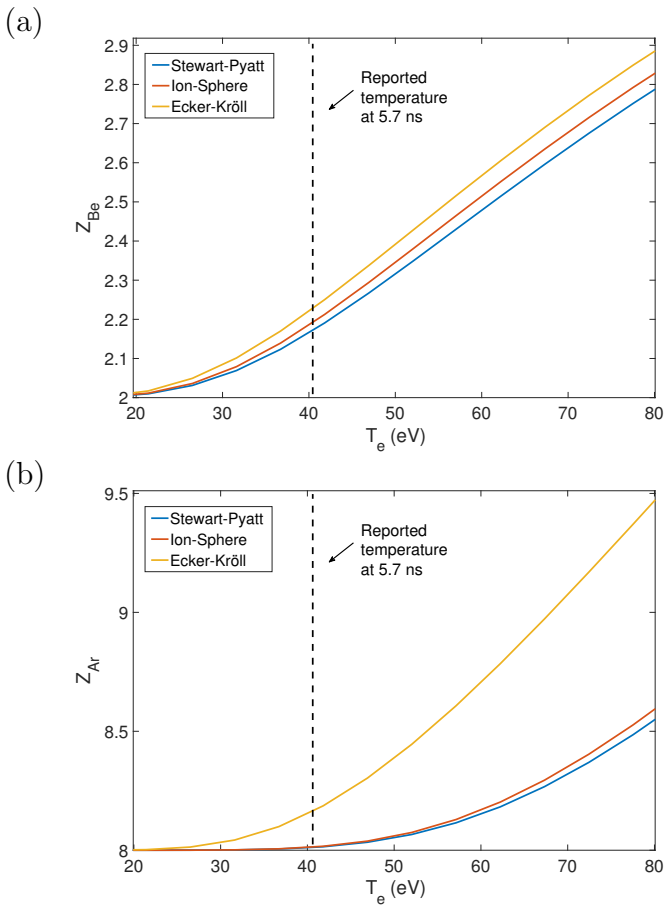

Figure 7: (Color online) Cretin simulations of Z_{Be} (a) and Z_{Ar} (b) vs. electron temperature for three different models of IPD, assuming a constant electron density of 1.9×10^{24} cm^{-3} and $\mu_{Ar} = 0.75 at.\%$. The temperature of the spectrum at 5.7 ns, 41 eV, is noted by the vertical dashed line.

inelastic scattering from bound electrons [18].

The χ^2 plot in Figure 6 shows that the elastic scattering strength is much more sensitive to beryllium K-shell ionization than to argon L-shell ionization. As discussed above, the elastic scattering does not change for Ar ionizations below $Z_{Ar} \leq 8$. Argon would have to ionize to $Z_{Ar} = 15$ if we fixed the beryllium ionization to the Cretin-predicted value of $Z_{Be} = 2.2$ (noted by the second marker in Figure 6). However, we consider values of $Z_{Ar} > 9.5$ to be unphysical; Figure 7 shows that the temperatures required to ionize argon beyond $Z_{Ar} = 9.5$ are over two times higher than the inferred

temperature of 41 eV. This is true even for the most extreme IPD model considered: Ecker-Kröll. In order for the Cretin simulations to report a Be ionization of 2.5, the temperature would need to be increased by 50%, which is well beyond the experimental error. We thus conclude that we measure a higher Be charge state than is predicted by the widely used ionization models that we tested. However, more experiments are needed to discern a more precise temperature dependence of beryllium K-shell ionization.

5. Conclusions and Outlook

We have investigated the influence of argon impurities in samples of warm dense beryllium on the elastic scattering strength as measured by XRTS. We find that even small amounts of argon can have a significant effect on the elastic scattering strength in XRTS spectra. This influence arises from the larger number of bound electrons in argon as well as the tighter bounds of the electrons, which stretches the atomic form factor further out into k-space. It is therefore of high importance to characterize carefully targets with respect to mid- and high-Z impurities to interpret the elastic feature of XRTS spectra properly.

On the other hand, we have demonstrated that under suitable experimental geometries and plasma conditions the mid-Z impurity content can be inferred from the elastic scattering strength. The analysis of the elastic scattering contribution in the spectra taken by Kritcher et al. [18] allowed for a precise determination of the argon content as 0.75 ± 0.2 at.%, which is consistent with the capsule production process. Because of the large scattering angle used here, the elastic scattering only probes the K- and L-shell occupation of argon, and is therefore insensitive to the argon ionization states of $Z_{Ar} \leq 8$. For the plasma conditions present in this study we do not expect significant ionization into the L-shell. In principle, a combination of backward and forward scattering XRTS measurements could probe all atomic shells of argon and thus yield valuable data for its ionization in the warm dense environment created by the compressed beryllium.

Our analysis describes a potential method to study the ionization balance of mid- and high-Z elements at extreme conditions by doping a small well-characterized impurity fraction into a low-Z host material. Ideally, such experiments should first be conducted with pure beryllium capsules to determine the plasma parameters in the compressed sample. Then the experiment could be repeated with capsules containing a known mid- or high-Z impurity

of interest and study its ionization balance under these conditions. A larger laser like, e.g., the National Ignition Facility (NIF) [38] could ionize the mid-Z element further into the L- or even the K-shell. Such experiments would avoid challenges arising from the high opacities of such elements when being highly compressed in a pure state. Our results demonstrate that the elastic scattering strength in XRTS measurements of compressed, doped beryllium provides the opportunity to test theoretical models for the ionization balance in warm and hot dense matter.

Acknowledgements

We thank the LLE and OMEGA laser staff for experimental support. We also thank Walter Johnson, Joe Nilsen, and Michael MacDonald for many fruitful discussions on elastic x-ray scattering, and Howard Scott for his tutelage on Cretin. This work was performed with the assistance of Lawrence Livermore National Laboratory (LLNL) under Contract No. DE-AC52-07NA27344 and supported by Laboratory Directed Research and Development (LDRD) Grant No. 18-ERD-033. SLAC HED is supported by DOE Fusion Energy Sciences FWP 100182. This work also performed under the Stewardship Science Graduate Fellowship program support Contract DE-NA0002135, and under the auspices of the U.S. Department of Energy by General Atomics under Contracts DE-NA0001808 and DE-AC52-06NA27279.

References

[1] T. Guillot, Science **286**, 72 (1999).

[2] B. Militzer, W. B. Hubbard, J. Vorberger, I. Tamblyn, and S. A. Bonev, The Astrophysical Journal Letters **688**, L45 (2008).

[3] N. Nettelmann, K. Wang, J. Fortney, S. Hamel, S. Yellamilli, M. Bethkenhagen, and R. Redmer, Icarus **275**, 107 (2016).

[4] R. Püstow, N. Nettelmann, W. Lorenzen, and R. Redmer, Icarus **267**, 323 (2016).

[5] J. D. Lindl, P. Amendt, R. L. Berger, S. G. Glendinning, S. H. Glenzer, S. W. Haan, R. L. Kauffman, O. L. Landen, and L. J. Suter, Physics of Plasmas **11**, 339 (2004).

[6] V. E. Fortov, *Extreme State of Matter on Earth and in the Cosmos*, Springer, 2011.

[7] O. A. Hurricane, D. A. Callahan, D. T. Casey, P. M. Celliers, C. Cerjan, E. L. Dewald, T. R. Dittrich, T. Döppner, D. E. Hinkel, L. F. B. Hopkins, J. L. Kline, S. L. Pape, T. Ma, A. G. MacPhee, J. L. Milovich, A. Pak, H.-S. Park, P. K. Patel, B. A. Remington, J. D. Salmonson, P. T. Springer, and R. Tommasini, Nature **506**, 343 (2014).

[8] S. H. Glenzer and R. Redmer, Rev. Mod. Phys. **81**, 1625 (2009).

[9] O. Ciricosta et al., Phys. Rev. Lett. **109**, 065002 (2012).

[10] D. J. Hoarty, P. Allan, S. F. James, C. R. D. Brown, L. M. R. Hobbs, M. P. Hill, J. W. O. Harris, J. Morton, M. G. Brookes, R. Shepherd, J. Dunn, H. Chen, E. Von Marley, P. Beiersdorfer, H. K. Chung, R. W. Lee, G. Brown, and J. Emig, Phys. Rev. Lett. **110**, 265003 (2013).

[11] B. J. B. Crowley, High Ener. Dens. Phys. **13**, 84 (2014).

[12] L. B. Fletcher, A. L. Kritcher, A. E. Pak, T. Ma, T. Döppner, C. Fortmann, L. Divol, O. S. Jones, O. L. Landen, J. Vorberger, D. Chapman, D. O. Gericke, B. Mattern, G. T. Seidler, G. Gregori, R. W. Falcone, and S. H. Glenzer, Phys. Rev. Lett. **112**, 145004 (2014).

[13] S. M. Vinko, O. Ciricosta, and J. S. Wark, Nat. Commun. **5**, 3533 (2014).

[14] C. A. Iglesias, High Ener. Dens. Phys. **12**, 5 (2014).

[15] C. A. Iglesias, High Ener. Dens. Phys. **7**, 38 (2011).

[16] S. H. Glenzer, G. Gregori, R. W. Lee, F. J. Rogers, S. W. Pollaine, and O. L. Landen, Phys. Rev. Lett. **90**, 175002 (2003).

[17] H. J. Lee, P. Neumayer, J. Castor, T. Döppner, R. W. Falcone, C. Fortmann, B. A. Hammel, A. L. Kritcher, O. L. Landen, R. W. Lee, D. D. Meyerhofer, D. H. Munro, R. Redmer, S. P. Regan, S. Weber, and S. H. Glenzer, Phys. Rev. Lett. **102**, 115001 (2009).

[18] A. Kritcher, T. Döppner, C. Fortmann, T. Ma, O. L. Landen, R. Wallace, and S. H. Glenzer, Phys. Rev. Lett. **107**, 015002 (2011).

[19] S. H. Glenzer, O. L. Landen, P. Neumayer, R. W. Lee, K. Widmann, S. W. Pollaine, R. J. Wallace, G. Gregori, A. Höll, T. Bornath, R. Thiele, V. Schwarz, W.-D. Kraeft, and R. Redmer, Phys. Rev. Lett. **98**, 065002 (2007).

[20] P. Neumayer, C. Fortmann, T. Döppner, P. Davis, R. W. Falcone, A. L. Kritcher, O. L. Landen, H. J. Lee, R. W. Lee, C. Niemann, S. L. Pape, and S. H. Glenzer, Phys. Rev. Lett. **105**, 075003 (2010).

[21] T. Döppner, O. Landen, H. Lee, P. Neumayer, S. Regan, and S. Glenzer, High Ener. Dens. Phys. **5**, 182 (2009).

[22] D. Riley, N. C. Woolsey, D. McSherry, I. Weaver, A. Djaoui, and E. Nardi, Phys. Rev. Lett. **84**, 1704 (2000).

[23] T. Ma, T. Döppner, R. W. Falcone, L. B. Fletcher, C. Fortmann, D. O. Gericke, O. L. Landen, H. J. Lee, A. Pak, J. Vorberger, K. Wünsch, and S. H. Glenzer, Phys. Rev. Lett. **110**, 065001 (2013).

[24] L. B. Fletcher, H. J. Lee, T. Döppner, E. Galter, B. Nagler, P. Heimann, C. Fortmann, S. L. Pape, T. Ma, M. Millot, A. Pak, D. Turnbull, D. A. Chapman, D. O. Gericke, J. Vorberger, T. White, G. Gregori, M. Wei, B. Barbrel, R. W. Falcone, C.-C. Kao, H. Nuhn, J. Welch, U. Zastrau, P. Neumayer, J. B. Hastings, and S. H. Glenzer, Nat. Photonics **9**, 274 (2015).

[25] D. Kraus, J. Vorberger, D. O. Gericke, V. Bagnoud, A. Blažević, W. Cayzac, A. Frank, G. Gregori, A. Ortner, A. Otten, F. Roth, G. Schaumann, D. Schumacher, K. Siegenthaler, F. Wagner, K. Wünsch, and M. Roth, Phys. Rev. Lett. **111**, 255501 (2013).

[26] D. A. Chapman, J. Vorberger, L. B. Fletcher, R. A. Baggot, L. Divol, T. Döppner, R. W. Falcone, S. H. Glenzer, G. Gregori, T. M. Guymer, A. L. Kritcher, O. L. Landen, T. Ma, A. E. Pak, and D. O. Gericke, Nat. Commun. **6**, 6839 (2015).

[27] D. Kraus, D. A. Chapman, A. L. Kritcher, R. A. Baggott, B. Bachmann, G. W. Collins, S. H. Glenzer, J. A. Hawreliak, D. H. Kalantar, O. L. Landen, T. Ma, S. Le Pape, J. Nilsen, D. C. Swift, P. Neumayer, R. W. Falcone, D. O. Gericke, and T. Döppner, Phys. Rev. E **94**, 011202 (2016).

[28] K. Wünsch, J. Vorberger, G. Gregori, and D. O. Gericke, EPL **94**, 25001 (2011).

[29] J. Chihara, J. Phys. F: Met. Phys. **17**, 295 (1987).

[30] G. Gregori, S. H. Glenzer, W. Rozmus, R. W. Lee, and O. L. Landen, Phys. Rev. E. **67**, 026412 (2003).

[31] K. Wünsch, P. Hilse, M. Schlanges, and D. O. Gericke, Phys. Rev. E **77**, 056404 (2008).

[32] R. Bredow, T. Bornath, W. Kraeft, and R. Redmer, Contrib. Plasma Phys. **53**, 276 (2013).

[33] D. A. Chapman, *Probing the Dynamic Structure of Dense Matter Using X-Ray Scattering*, PhD thesis, University of Warwick, 2015.

[34] D. A. Chapman, *User guide and theoretical basis for the Multi-Component Scattering Spectra (MCSS) Thomson scattering analysis code (O) - AWE Report 12/17*, AWE, 2017.

[35] L. Pauling and J. Sherman, Zeitschr. Kristallogr. **1**, 81 (1932).

[36] G. E. Engel and B. Farid, Phys. Rev. B **47** (1993).

[37] J. C. Stewart and K. D. Pyatt, Astrophys. J. **144**, 1203 (1966).

[38] E. I. Moses, J. Phys. Conf. Ser. **112**, 012003 (2008).